**RESEARCH ARTICLE**

# Segregation-controlled densification and grain growth in rare earth-doped $Y_2O_3$

**Moritz Kindelmann[1,2]** | **Ke Ran[3,4]** | **Wolfgang Rheinheimer[1]** | **Koji Morita[5]** | **Joachim Mayer[3,4]** | **Martin Bram[1]** | **Olivier Guillon[1,2,6]**

[1]Forschungszentrum Jülich GmbH, Institute of Energy and Climate Research, Materials Synthesis and Processing (IEK-1), Jülich, Germany

[2]Institute of Mineral Engineering, RWTH Aachen University, Aachen, Germany

[3]Central Facility for Electron Microscopy (GFE), RWTH Aachen University, Aachen, Germany

[4]Forschungszentrum Jülich GmbH Ernst Ruska-Centre for Microscopy and Spectroscopy with Electrons (ER-C), Jülich, Germany

[5]National Institute for Materials Science, Tsukuba, Japan

[6]Jülich Aachen Research Alliance, JARA-Energy, Jülich, Germany

**Correspondence**

Moritz Kindelmann, Forschungszentrum Jülich GmbH, Institute of Energy and Climate Research, Materials Synthesis and Processing (IEK-1), 52425 Jülich, Germany.
Email: m.kindelmann@fz-juelich.de

**Abstract**

Cation doping of $Y_2O_3$ is an established approach for tailoring densification and grain growth during sintering. However, the segregation of doped cations to the grain boundary and their impact on processing are still not completely understood. Segregation can be driven by electrostatic effects due to charge mismatch with the host lattice or elastic effects induced by ion size mismatch. While segregation is caused by thermodynamics, it impacts diffusion and the kinetics of grain boundaries during densification and microstructure evolution. In this study, we utilize two isovalent dopants ($La^{3+}$ and $Gd^{3+}$), that is we focus on the elastic component of segregation. We investigate the densification as well as the grain growth kinetics of both doped and undoped $Y_2O_3$ during field-assisted sintering/spark plasma sintering (FAST/SPS). While $Gd^{3+}$ is showing no significant effect on densification, $La^{3+}$ resulted in a strongly reduced sintering activity. Furthermore, the analysis of the grain growth behavior during sintering and on predensified samples revealed a decrease in the grain growth coefficient, with $La^{3+}$ having the strongest impact. The structure and chemistry at the grain boundary were observed by aberration-corrected TEM. While no structural change was caused by doping, the chemical analysis showed a strong segregation of $La^{3+}$ to the grain boundary, which could not be observed for $Gd^{3+}$. The results indicate that segregated $La^{3+}$ causes a drastic decrease in grain boundary migration rates through solute drag as well as much slower sintering kinetics, likely caused by a decrease in the grain boundary self-diffusion due to segregation. This study further underlines the importance of the elastic contribution to cation segregation and establishes a clear relationship to grain growth and sintering kinetics, which are both decreased by segregation.

**KEYWORDS**
doping, grain growth, segregation, sintering, solute drag, spark plasma sintering, yttria

# 1 | INTRODUCTION

The segregation of alloy species to grain boundaries is well known from metals and well investigated due to its potential for the stabilization of nanocrystalline microstructures.[1–3] For ceramics, segregation is known since a long time but not well investigated due to the higher complexity. While segregation in metals is purely driven by elastic effects due to a size mismatch of the species with respect to the host lattice, electrostatic effects become important in ceramics as caused by the charge mismatch of dopants.[4,5] Adjacent to the grain boundary core with segregated dopants, space charge may form compensating the charge of the boundary core.[6–8] Accordingly, our knowledge on segregation in ceramics is mostly limited to a few model systems. For zirconia, segregation of $Y^{3+}$ and other dopants can dominate microstructure evolution and oxygen conductivity.[9–12] These studies also investigated the elastic and electrostatic contributions to segregation. For $Al_2O_3$ and $Si_3N_4$, segregation and formation of nanometer-sized amorphous layers at grain boundaries were studied in detail.[13,14] Especially $Al_2O_3$ revealed a pronounced segregation of doped Y and La leading to lower densification rates and grain growth kinetics.[15]

This study focusses on segregation in yttria, which is an important material for harsh environments as, for example, in plasma etching devices for semiconductor processing.[16–18] Sintering yttria to high density generally requires very high temperatures (up to 2000°C) for several hours.[19,20] To lower sintering temperatures, doping is commonly used. Particularly, transparent $Y_2O_3$ ceramics can only be achieved by a combination of doping and applied mechanical pressure.[21–23] As such, yttria is a well-suited model system for detailed analysis of segregation and its impact on microstructure evolution.

Several authors established cation doping in $Y_2O_3$ as a strategy to improve sintering and microstructure evolution. Various divalent (CaO, MgO, and SrO [24,25]), trivalent ($La_2O_3$[20]), and tetravalent cations ($TiO_2$, $SiO_2$, $CeO_2$, $ThO_2$, and $ZrO_2$[26–28]) were initially investigated to realize improved processing properties. These early studies indicate the two main strategies for promoting the densification of $Y_2O_3$: (I) Generating a drag force on grain boundary migration by including tetravalent ($Th^{4+}$, $Zr^{4+}$) or trivalent ($La^{3+}$) cations. The drag force is either caused by the dopant segregation along the grain boundaries (solute drag) or by the occurrence of a transient solid second phase at very high temperatures resulting in Zener pinning. (II) Improving the densification behavior by including divalent cations ($Ca^{2+}$, $Mg^{2+}$, $Sr^{2+}$) or selected tetravalent cations ($Ti^{4+}$)—The cations generate an increased defect concentration which eases diffusion and densification.

The first comprehensive analysis of the influence of doping on the grain growth behavior in yttria was conducted by Chen and Chen.[29,30] Based on the assumption that cation diffusivity is the controlling mechanism for grain boundary mobility in the $Y_2O_3$ system, it was concluded that the grain boundary mobility is accelerated by acceptor dopants (divalent cations) and is inhibited by donor dopants (tetravalent, pentavalent cations).[31] Additionally, cations with a large size mismatch ($Ti^{4+}$, $Nb^{5+}$) showed a positive effect on grain boundary mobility, which could not be attributed to defect chemical effects. The positive influence of trivalent dopants ($La^{3+}$, $Gd^{3+}$, $Sc^{3+}$, $Yb^{3+}$) could not be associated with defect chemistry as well and was therefore linked to lattice distortions induced by differences of ionic radii[29] In these works, authors did not come to a final conclusion on the influence of trivalent dopants on the grain boundary mobility. This profound understanding of grain boundary mobility control by adding suitable dopants enabled exact microstructure control and facilitated the two-step sintering method. Based on this method, almost complete densification of $Y_2O_3$ without grain growth in the final stage of sintering was demonstrated.[32,33]

The first comprehensive study on the influence of doping on the sinterability of $Y_2O_3$ was conducted by Kodo et al.[34] This work focused on co-doping of $Y_2O_3$ with 1Ni/1Er and 1Mn/1Er (in wt. %), which allowed a strong reduction of the sintering temperature from 1600 to 1300°C while maintaining high relative densities. Further systematic studies investigated the influence of cations with different valency on the densification, considering divalent[35] and trivalent as well as tetravalent cations.[36] As some cations tend to segregate along the grain boundaries, local changes in the oxygen vacancy concentration (for divalent cations) as well as lattice distortions and changes in the ionicity of the oxygen anion are discussed to induce the observed doping effects.[28,29]

Despite intense research into the advantage of cation doping to produce highly dense $Y_2O_3$, an application of FAST/SPS for consolidation of doped $Y_2O_3$ is rarely discussed. Yoshida investigated $Y_2O_3$ doped with 1 mol.% $Zn^{2+}$,[22] which enabled the use of very low sintering temperatures (870–900°C) at high uniaxial pressures (up to 170 MPa). Furuse et al. investigated the influence of 1 to 50 mol.% $Yb^{3+}$ doping into $Y_2O_3$ during FAST/SPS processing leading to highly dense laser ceramics.[23]

Particularly for plasma etching applications, yttria ceramics show major advantages due to their high resistance to harsh environments. Due to the lowered plasma resistance induced by residual porosity, high relative densities are required for these applications.[18,37,38] Although several dopants, which can improve the final relative density, have been reported in previous studies, severe restrictions regarding permissible elements in the semiconductor industry prevent an application of doped $Y_2O_3$ to date. Most of the highly effective dopants, including transition metal cations like $Ni^{2+}$ and $Zn^{2+}$, are not allowed due to their incompatibility with the plasma chemistry. Nevertheless,

exceptions can be made for doping with rare earth metal ions from the lanthanide group, which are classified to be uncritical at low concentrations for an application in plasma etching processes.

This study aims on investigating the impact of segregation on sintering and grain growth in yttria. Segregation engineering is used to reveal the impact of the elastic contributions to segregation. Two different dopants with no charge mismatch (i.e., isovalent) were used. One of them ($Gd^{3+}$) has almost no size mismatch with respect to $Y^{3+}$, while the other ($La^{3+}$) is significantly larger. Both dopants are stable against a valency changes (unlike $Eu^{3+}$ [21]). Sintering kinetics during FAST/SPS were analyzed. $Gd^{3+}$ doping (no size mismatch) did not change sintering significantly, while $La^{3+}$ doping (with size mismatch) resulted in strongly reduced sintering kinetics. A detailed grain growth study of presintered samples allowed extracting grain growth coefficients and revealed much slower grain growth kinetics for La doping. The structure and chemistry were observed by aberration-corrected TEM. The structure of the grain boundaries was not changed by doping and was highly ordered for all compositions. However, the chemical analysis shows a strong segregation of $La^{3+}$ to the grain boundaries, while no segregation was visible for $Gd^{3+}$ doping. This agrees well with the expectations, as only $La^{3+}$ has a significant size mismatch with the host lattice.

From the results, it is evident that segregated $La^{3+}$ causes a drastic decrease in grain boundary migration rates, that is solute drag. Beyond solute drag, sintering is impacted by segregation as well: much slower sintering kinetics were observed for $La^{3+}$ doping. This is likely caused by a decrease in the grain boundary self-diffusion due to cation segregation, which is well-known for metals [39]. Furthermore, in the case of doped samples, the formation of nanopores on grain boundaries caused by processing-related effects is discussed as another possible reason for retarding grain growth.

## 2 | EXPERIMENTAL PROCEDURE

Throughout this study, high-purity $Y_2O_3$ powder (99.99% purity, KDL Resources) was used as a starting material and the nitrate salts $La(NO_3)_3 * 6 H_2O$ (99.99% purity, Sigma Aldrich) and $Gd(NO_3)_3 * 6 H_2O$ (99.99% purity, Sigma Aldrich) were applied as dopant sources. $Y_2O_3$ powers were doped with 1 mol% $La^{3+}$ and 1 mol% $Gd^{3+}$. Therefore,

powders were prepared by ball milling the starting powder together with the respective nitrate in ethanol for 24 h adding TZP balls. After milling, the powders were dried in a furnace for 24 h at 80°C and afterward heated in air for 2 h at 600°C. As a reference, undoped $Y_2O_3$ powder was processed using the same procedure to achieve comparable powder properties. Before sintering, all powders were sieved through a 100-μm mesh to remove large agglomerates. The median agglomerate size $d_{50}$ of all powders was between $2.0 \pm 0.1$ and $2.4 \pm 0.1$ μm, while the primary particle size was estimated by transmission electron microscopy (TEM) to be in the range of $60 \pm 17$ nm. The elemental composition after powder processing was measured using inductively coupled plasma mass spectrometry (ICP-MS, Agilent 7900) and is displayed in Table 1. All powders have a low amount of chemical impurities, especially for critical elements that have been shown to influence the densification and grain growth behavior.[29,36]

All sintering experiments were performed in a FAST/SPS device (SPS-1050, Fuji Electronic Industrial Co., Ltd.) using a graphite tool with Ø 20 mm diameter. The die was capsuled by graphite felt to reduce thermal radiation from the die surfaces. Graphite sheets were used to separate the powder sample from the pressing tools. Furthermore, the sheets improve the heat transfer and ease the removal of the sample from the die. All sintering cycles were done using a uniaxial pressure of 50 MPa, a heating rate of 100 K/min. Furthermore, the FAST/SPS chamber was evacuated to <0.5 mbar during the whole cycle. The sintering temperature was controlled by using a radial pyrometer focused on the outer surface of the die through a hole in the graphite felt. Two kinds of sintering experiments were conducted to investigate the densification behavior as well as grain growth during the FAST/SPS processing: (I) The densification behavior was investigated by varying the sintering temperature from 1100 to 1400°C in 50°C steps, while keeping the heating rate (100 K/min), dwell time (10 min), and applied pressure (50 MPa) constant. (II) The grain growth behavior during FAST/SPS was investigated at a sintering temperature of 1400°C by varying the dwell time between 0, 30, 60, and 120 min. All other sintering parameters were kept constant.

After removal from the pressing tool, graphite sheet residues were removed by a thermal treatment at 900°C for 2 h in air. To investigate the densification behavior (I), the density of all samples was measured by the Archimedes method in

**TABLE 1** Elemental composition of the prepared powders measured by ICP-MS

| | $Mg^{2+}$ | $Sr^{2+}$ | $Zn^{2+}$ | $Ni^{2+}$ | $Al^{3+}$ | $Ga^{3+}$ | $La^{3+}$ | $Gd^{3+}$ | $Ti^{4+}$ | $Zr^{4+}$ | $Si^{4+}$ | $Nb^{5+}$ |
|---|---|---|---|---|---|---|---|---|---|---|---|---|
| $Y_2O_3$ | 0.62 | 0.053 | 0.97 | <0.2 | 1.1 | 0.036 | <8 | <10 | 0.21 | 12.1 | <40 | <0.004 |
| $1LaY_2O_3$ | 0.87 | 0.076 | 1.12 | <0.2 | 1.1 | 0.11 | 9150 | <10 | 0.17 | 8.8 | <50 | <0.005 |
| $1GdY_2O_3$ | 2.12 | 0.094 | 2.36 | <0.2 | 2.11 | <0.3 | 17 | 13600 | 0.37 | 7.3 | <40 | <0.004 |

_Note:_ All values are displayed in mg/kg.

deionized water and the relative density was calculated using 5.03 g/cm$^3$ as the theoretical density of $Y_2O_3$.[40]

All cross-sections of samples were metallographically ground and afterward polished to obtain a mirror-like surface and thermally etched for 1 h at 1100°C in air to reveal the grain structure. The microstructure was investigated by scanning electron microscopy (SEM, Zeiss Cross Beam XB540). For consistency, investigation was done on a fixed position in the cross-section of samples, which was close to the position of the pyrometer. The grain size was analyzed using the average linear intercept method. For determining the average grain size, at least 250 grains were considered and a correction factor of 1.6 was used.[41]

Additional to sintering experiments in the field-assisted sintering device, grain growth studies were conducted in air to determine the grain boundary mobility for doped and undoped $Y_2O_3$. Therefore, samples, which were densified by FAST/SPS at 1400°C to density >99.5%, were thermally treated in a muffle furnace for 10 h at temperature of 1400, 1500, and 1600°C.

In order to determine the grain boundary mobility, the general equation for grain growth was applied.[42]

$$G^n - G_0^n = Kt, \tag{1}$$

with

$$K = 2\alpha\gamma_{gb}M_{gb}, \tag{2}$$

where $G$ and $G_0$ are the average grain size at the time $t$ and $t_0$, respectively, $n$ is the grain growth exponent, and $K$ is a temperature-dependent growth factor including a geometrical factor $\alpha$, the grain boundary energy $\gamma_{gb}$, and the grain boundary mobility $M_{gb}$. As in the literature,[43] the growth coefficient was assumed to be $n = 2$ as expected for grain boundary migration controlled by the interface reaction.[42,44]

High-angle annular dark-field (STEM-HAADF) imaging and STEM-EDX were performed on TEM lamellas which were prepared and thinned by focused ion beam (FIB, FEI STRATA FIB 205). The lamellas were selected from FAST/SPS-processed samples from the same position where the grain size measurements were performed to allow a comparison between grain growth kinetics and the grain boundary structure. All STEM investigations were performed using an aberration-corrected transmission electron microscope (FEI Titan G2 80-200 ChemiSTEM) to investigate the grain boundary structure and the chemical composition at the atomic scale.

## 3 | RESULTS AND DISCUSSION

### 3.1 | Densification behavior

The densification behavior of doped and undoped $Y_2O_3$ powders was characterized in terms of the development of

relative density and grain size with increasing sintering temperatures from 1100 to 1400°C. Figure 1 displays the relative density as a function of the sintering temperature measured by the Archimedes method. The graph enables to draw two conclusions:

I Up to 1300°C, doping with 1 mol% $La^{3+}$ shows an impeding effect on the densification. The densification curve shifted by roughly 100 K to higher temperatures for achieving comparable relative densities to undoped $Y_2O_3$. At higher temperatures (1350 and 1400°C), the impeding effect of $La^{3+}$ became negligible. The impeding influence of $La^{3+}$ on the densification of $Y_2O_3$ was already discussed by Yoshida et al.[36] They correlated the retarded densification with the ionic bonding strength formed around the dopant.

II In contrast to $La^{3+}$, $Gd^{3+}$ doping did not have any measurable influence on the densification behavior despite having comparable physical and chemical properties to $La^{3+}$ with respect to valence and energy of the valence electron orbitals.[36] As discussed by Langer et al., for submicron-sized alumina powders, the rate-controlling densification mechanism active during FAST/SPS consolidation with comparable processing parameters (heating rate from 10 to 150 K/min, uniaxial pressure from 15 to 50 MPa) is grain boundary diffusion.[45,46] Provided that this also applies to $Y_2O_3$, our results suggest a different influence of La and Gd doping on the grain boundary diffusion during densification by FAST/SPS: As discussed below, this is likely caused by a different segregation behavior.
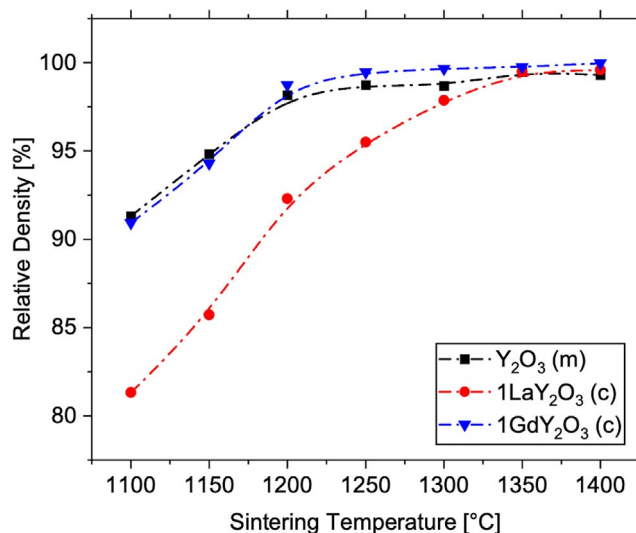


**FIGURE 1** Development of relative density as a function of the sintering temperature during FAST/SPS. Dwell time (10 min) and applied pressure (50 MPa) were kept constant for all samples. Lines are added to guide the eye [Color figure can be viewed at wileyonlinelibrary.com]

This assumption is confirmed by the development of average grain sizes as a function of temperature (Figure 2) and relative density (Figure 3). Both dopants retarded grain coarsening during early stage sintering leading to smaller grain sizes throughout the whole investigated temperature range. With respect to retarded grain growth, $La^{3+}$ cations had a larger impact compared to $Gd^{3+}$ cations. Additionally, grain growth during densification was gradually decreased with increasing sintering temperature. Again, doping with $La^{3+}$ displayed the stronger effect.

To conclude this section, the development of grain size as a function of relative density (Figure 3) reveals two overlapping effects observable during the densification of $La^{3+}$- and $Gd^{3+}$-doped $Y_2O_3$. Both dopants lead to a specific reduction of grain growth during densification, while doping with $Gd^{3+}$ does not influence the densification compared to undoped $Y_2O_3$ (see Figure 1). In contrast, doping with $La^{3+}$ also leads to a retarded densification, which hints on a change of grain boundary diffusion mechanism as specific characteristic of $La^{3+}$ doping. The comparison of sintering trajectories for $La^{3+}$- and $Gd^{3+}$-doped $Y_2O_3$ (Figure 3) reveals similar grain coarsening behavior during densification, an effect which is obviously decoupled from the lower sintering activity in the case of $La^{3+}$ doping.

## 3.2 | Grain growth kinetics

For better understanding how rare earth doping impacts grain boundary mobility, isothermal grain growth studies were conducted in the FAST/SPS device at 1400°C. Therefore,
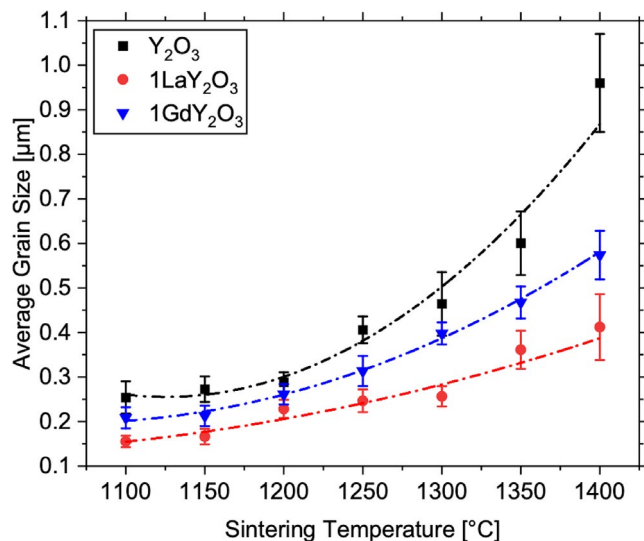
samples were sintered to almost full density by FAST/SPS and the dwell time was varied between 0 and 120 min. Figure 4 shows the development of the average grain size depending on dwell time. In these experiments, both dopants show a drag effect onto the grain boundary migration leading to a retarded grain growth. Comparable to the densification in Section 3.1, the effect was much stronger for $La^{3+}$ doping compared to $Gd^{3+}$ doping. As discussed later in detail,
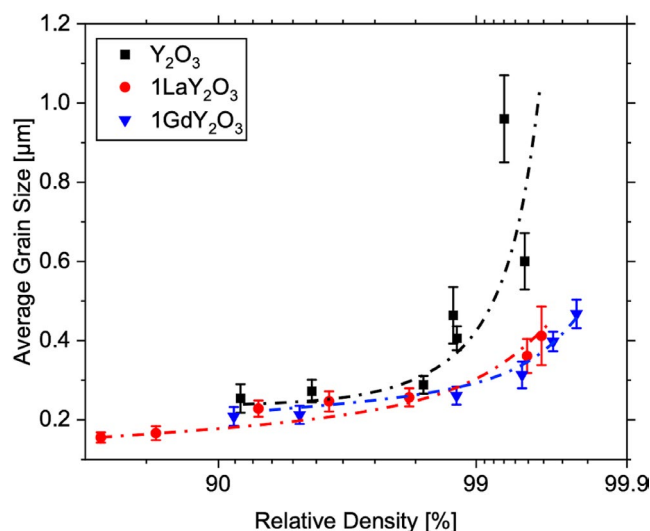


**FIGURE 3** Sintering trajectory displaying the average grain size development as a function of the relative density during FAST/SPS. Dwell time (10 min) and applied pressure (50 MPa) were kept constant for all data points. Lines are added to guide the eye [Color figure can be viewed at wileyonlinelibrary.com]
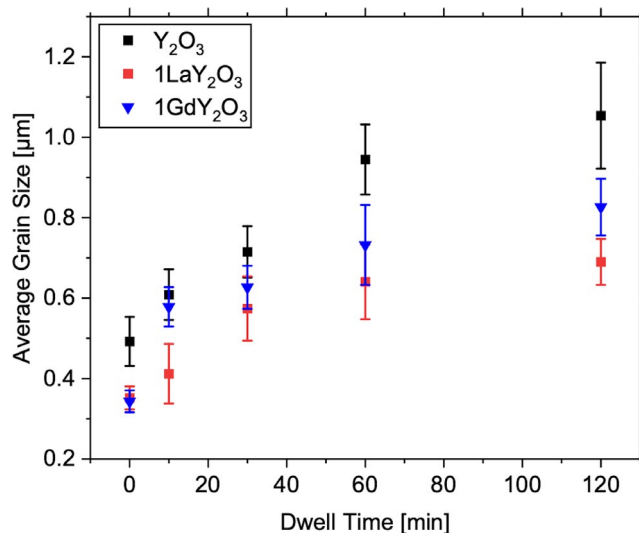


**FIGURE 2** Development of the average grain size as a function of the sintering temperature during FAST/SPS. Dwell time (10 min) and applied pressure (50 MPa) were kept constant for all samples. Lines are added to guide the eye [Color figure can be viewed at wileyonlinelibrary.com]



**FIGURE 4** Development of the average grain size as a function of dwell time at 1400°C in the FAST/SPS device under a uniaxial pressure of 50 MPa. Doping with $La^{3+}$ and $Gd^{3+}$ caused a gradual decrease in grain growth with $La^{3+}$ having the larger drag effect [Color figure can be viewed at wileyonlinelibrary.com]

these results indicate that $Y_2O_3$ doped with rare earth cations experiences solute drag on grain boundary motion. Several TEM studies on $Y_2O_3$-based materials showed a segregation of doping elements in the vicinity of grain boundaries, which is an important detail to understand their influence on grain boundary motion during isothermal treatments at elevated temperatures. EDX measurements with TEM showed that dopants ($Al^{3+}$, $Ni^{2+}$, $Zn^{2+}$) in conventionally sintered $Y_2O_3$ segregate to the core of the grain boundary where they influence densification and grain boundary motion.

To further quantify the solute drag effect induced by $La^{3+}$ doping, heat treatments in a muffle furnace at 1400, 1500, and 1600°C were conducted to measure the grain boundary mobility of undoped $Y_2O_3$ and $Y_2O_3$ doped with 1 mol. % $La^{3+}$ in air. Figure 5 shows the grain boundary mobility obtained from Equation (2) and the measured mean grain sizes as Arrhenius plot. In the investigated temperature range, $La^{3+}$-doped $Y_2O_3$ showed a lower grain boundary mobility in comparison to undoped $Y_2O_3$. Again, this result indicates a solute drag effect, which is expected to be caused by cation segregation at the grain boundaries. The activation energy was derived from the slope of the linear fit in Figure 5. The activation energy for pure $Y_2O_3$ is comparable to other studies investigating FAST/SPS sintering of $Y_2O_3$.[47,48] However, activation energy values determined on conventionally sintered $Y_2O_3$ samples were reported to be in the range between 340 and 399 kJ/mol,[29,49] which might be caused by a different atmosphere, for example without carbon. In Figure 5, the introduction of $La^{3+}$ cations leads to an increase in the activation energy. This is likely connected to dopant segregation to

the grain boundary and the resulting solute drag, which adds an additional temperature-dependent mechanism to the grain boundary migration.

Figure 6 shows SEM images of the microstructure of undoped and $La^{3+}$-doped $Y_2O_3$ after FAST/SPS sintering at 1400°C (Figure 6A,C) and after thermal treatment in a muffle furnace in air at 1500°C for 10 h. Before the heat treatment, both samples displayed a similar fine-grained homogeneous microstructure although being processed with different dwell times for balancing the different rate of grain growth during densification (see Figure 3). After the annealing step at 1500°C in air, microstructure of undoped $Y_2O_3$ (Figure 6B) shows some coarsening. In comparison, La-doped $Y_2O_3$ led to a fine-grained microstructure (Figure 6D).

Additional to finer grain sizes, $La^{3+}$-doped $Y_2O_3$ displays an increased amount of intergranular porosity (Figure 6D) while undoped $Y_2O_3$ exhibits a noticeable amount of intragranular porosity (Figure 6B). Decreased grain boundary mobility during dwell time, which is induced by a solute drag effect of $La^{3+}$ doping, inhibited the pore detachment from the grain boundaries. Pinning of pores to the grain boundaries can be crucial to facilitate the removal of residual porosity during the final stage of sintering. While completely eliminating intragranular pores by lattice diffusion is mostly not possible due to slow diffusion kinetics, the removal of intergranular pores through grain boundary diffusion is still possible in the final stage of sintering. By tuning the sintering parameters in an accurate way, this effect can be advantageously used to eliminate residual porosity to an absolute minimum. It is expected that this strategy can foster further improvement in the resistance of $Y_2O_3$-based ceramics against erosion in harsh plasma environments.[18,37,38] Furthermore, this effect is attractive for producing transparent $Y_2O_3$ ceramics using FAST/SPS given that elimination of residual porosity is directly coupled to a reduced light scattering on microstructure defects.[50]

## 3.3 | Grain boundary structure and chemistry

For a thorough understanding of the effect of $La^{3+}$ and $Gd^{3+}$ doping on the sintering and coarsening behavior of $Y_2O_3$ during FAST/SPS, the characterization of structure and chemistry at the grain boundary are crucial. Therefore, STEM and STEM-EDS investigations of the grain boundaries in pure $Y_2O_3$, 1 mol% $LaY_2O_3$, and 1 mol% $GdY_2O_3$ (all sintered by FAST/SPS at 1400°C, 50 MPa, 120 min) were conducted. The HAADF images in Figure 7 display an overview of representative grain boundaries for all three compositions. The interface in pure $Y_2O_3$ shows no visible impurities, secondary
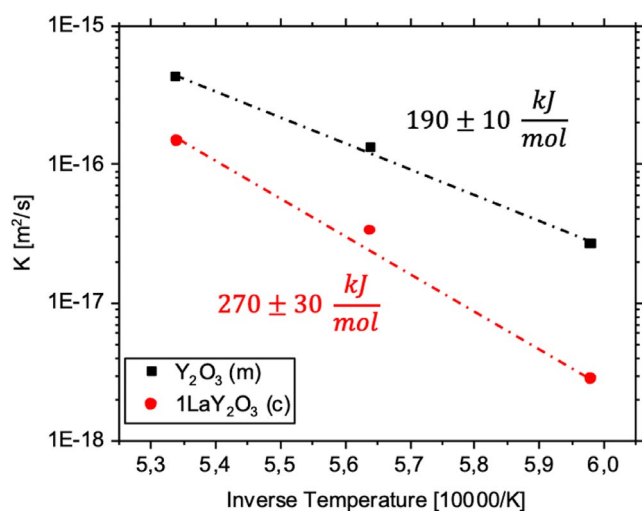


**FIGURE 5** Arrhenius plot for showing the grain growth factor K as a function of the inverse annealing temperature. All samples were almost fully densified by FAST/SPS before conducting the thermal treatment in air. The grain growth factor was calculated using Equation (1) with $n = 2$. The activation energy for grain growth is derived from the slope of the linear fit and shown next to the graph [Color figure can be viewed at wileyonlinelibrary.com]
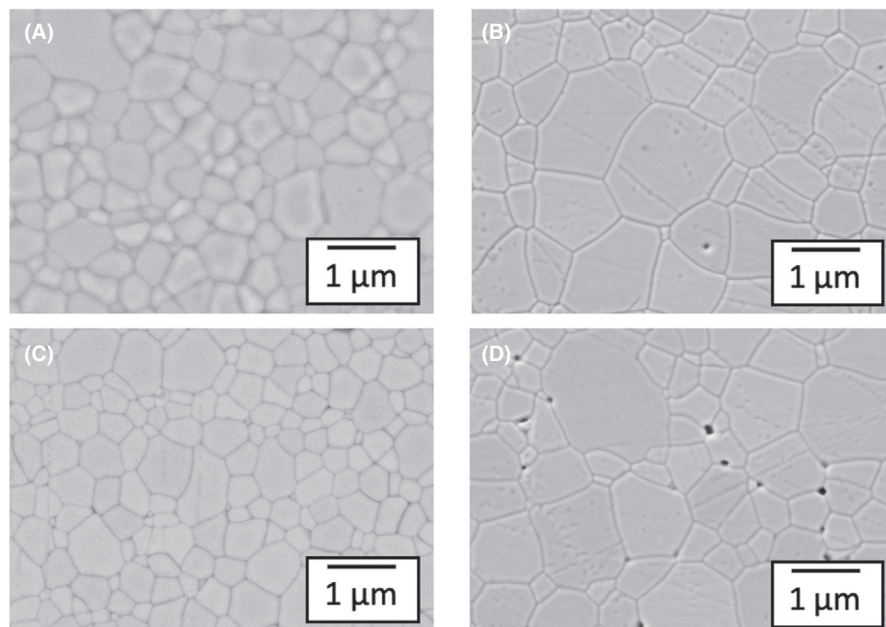
**FIGURE 6** SEM images of the microstructure of (A) $Y_2O_3$ sintered at 1400°C for 30 min using 50 MPa uniaxial pressure (GS: 0.61 µm ± 0.06 µm), (B) $Y_2O_3$ after thermal annealing at 1500°C for 10 h in air (GS: 1.22 µm ± 0.28 µm), (C) $Y_2O_3$ doped with 1 mol.% $La^{3+}$ sintered at 1400°C for 60 min using 50 MPa uniaxial pressure (GS: s0.57 µm ± 0.07 µm), (D) $Y_2O_3$ doped with 1 mol.% $La^{3+}$ after thermal annealing at 1500°C for 10 h in air (GS: 0.75 µm ± 0.11). All micrographs were taken at same position of sample cross-section
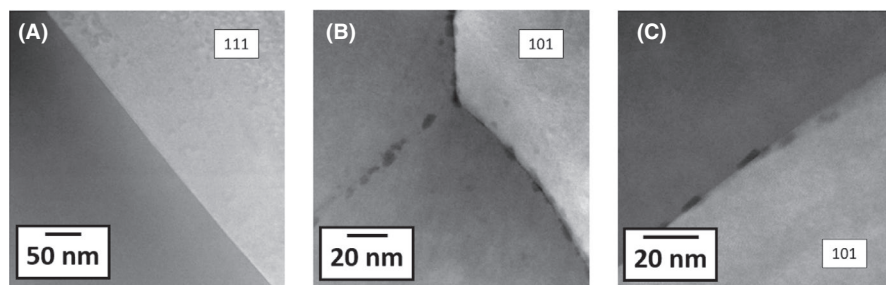


**FIGURE 7** HAADF overview images of the microstructure at the grain boundary of (A) $Y_2O_3$, (B) 1 mol% $LaY_2O_3$, and (C) 1 mol% $GdY_2O_3$ sintered by FAST/SPS (1400°C, 100 K/min, 50 MPa, 120 min)

phases, or defects (Figure 7A). Compared to pure $Y_2O_3$, both doped compositions exhibit dark areas located at the grain boundary. Compositions containing 1 mol% $La^{3+}$ show a higher number of dark domains along the grain boundary compared to 1 mol% $Gd^{3+}$ $Y_2O_3$ in Figure 8B,C. Due to the highly localized investigation during STEM, a profound conclusion on the number of nanodomains is difficult to draw. Nevertheless, pure $Y_2O_3$ samples did not show any secondary features at the grain boundary.

To further understand the structural and chemical change, an in-depth investigation of the grain boundaries was conducted. STEM investigations with atomic resolution were applied to reveal the interface structure and composition in pure and rare earth-doped $Y_2O_3$. Figure 8 shows the grain boundary structure and chemical composition of pure $Y_2O_3$. The HAADF image in Figure 8A displays a clean grain boundary with no structural defects or intergranular films present. Additional EDS elemental mappings at the atomic scale (Figure 8B,C) confirm the chemical and structural purity of the grain boundaries in FAST/SPS-sintered $Y_2O_3$. The EDS intensity of Y and O is dependent on the orientation of the crystallographic planes, leading to slight differences between the adjacent grains. This orientation effect is more

pronounced for heavier atoms as Y, La, and Gd (Figures 8B,C and 9B,D) in comparison to O.

Additionally, FAST/SPS-sintered 1 mol% $La^{3+}$ and 1 mol% $Gd^{3+}$-doped $Y_2O_3$ were investigated in the same manner to compare the influence of doping on the grain boundary structure and chemistry. The HAADF imaging and EDS mapping results of rare earth-doped $Y_2O_3$ are summarized in Figure 9. Equally to the interfaces in pure $Y_2O_3$, the rare earth-doped compounds exhibit no secondary phases or intergranular films at the grain boundary. Nevertheless, both micrographs display characteristic dark areas which were already observed in Figure 7B,C. A comparison between the dark areas visible in both micrographs and their corresponding EDX mappings reveals low elemental intensities for yttrium, oxygen as well as the corresponding dopant, which implies the presence of a nano-sized pores at the grain boundaries. This nanoporosity is located predominantly at the grain boundaries and the pores are arranged along the interface, which might lead to additional drag forces on the grain boundary movement during grain growth.

Furthermore, EDS mapping of the grain boundary in $La^{3+}$-doped $Y_2O_3$ reveals a clear segregation of the dopant species to the grain boundary (Figure 9B). This segregation
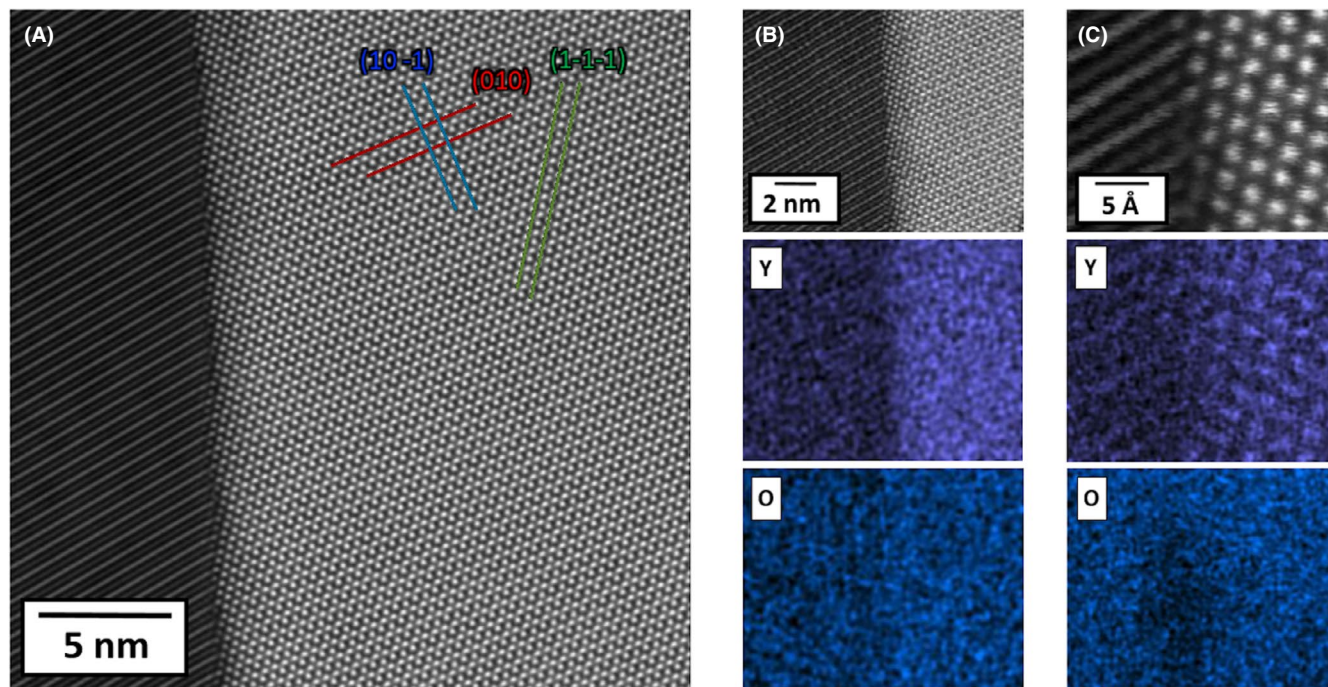
**FIGURE 8** Microstructure and chemical composition at the grain boundary of FAST/SPS-sintered pure $Y_2O_3$. (A) HAADF image showing a defect-free grain boundary, (B) STEM-EDX overview mapping, and (C) STEM-EDX detail [Color figure can be viewed at wileyonlinelibrary.com]

is comparable to several studies which showed a segregation of low amounts of different cations ($Mn^{2+}$, $Ni^{2+}$,[34] $Zn^{2+}$,[35] $Al^{3+}$ [36]) to the grain boundary in $Y_2O_3$. The direct comparison of the dopant distribution of $Gd^{3+}$ and $La^{3+}$-doped $Y_2O_3$ further highlights the different solution behavior of $Gd^{3+}$ cations in the $Y_2O_3$ lattice. No segregation of $Gd^{3+}$ cations to the grain boundary can be observed in the EDS mapping in Figure 9D. These differences in the segregation behavior of the investigated dopants seem to be the main influence which leads to the differing densification behavior during FAST/SPS sintering (Figure 1). A homogeneous distribution of cations in the $Y_2O_3$ lattice as for $Gd^{3+}$ doping seems to have no measurable influence onto the densification and therefore leads to a sintering behavior that is comparable to pure $Y_2O_3$, while $La^{3+}$ dopant segregation decelerates the densification process. Similar observation could be made for line scans, which reveal the pronounced segregation of La atoms and a homogeneous distribution of Gd (Figure 9E,F).

## 3.4 | Impact of segregation on sintering and grain growth

The segregation of dopants in ceramics is driven by a decrease in Gibbs free energy.[51] There are electrostatic and elastic contributions to this driving force for segregation stemming from a charge and size mismatch of the dopant with respect to the host lattice site.[4,5,8,24,52,53] While also important for aliovalent dopants, the size mismatch is the major factor for the segregation of isovalent dopants.[3,54] This behavior was observed by several studies on dopant segregation in TZP ceramics.[10–12] Similar results were found for $Y_2O_3$ by Yoshida et al., who showed a segregation of cations having a large ionic radii mismatch (divalent: $Ni^{2+}$, $Mn^{2+}$, $Zn^{2+}$ and trivalent: $Al^{3+}$, $Ge^{3+}$)[35,36] on grain boundaries and homogeneous distribution of dopants with almost the same radius inside the bulk ($Er^{3+}$).[34]

Here, we use two different isovalent dopants with different size mismatch. The cation sizes of dopants used in this study are 0.093, 0.094, and 0.106 nm for $Y^{3+}$, $Gd^{3+}$, and $La^{3+}$, respectively. Due to the very small size mismatch, $Gd^{3+}$ does not segregate to the grain boundaries and shows a very high solubility in $Y_2O_3$ (100% substitution possible[55]). In contrast, the large size mismatch of $La^{3+}$ results in a low solubility in the host lattice (7 mol%[56]) and strong segregation to the grain boundaries. This different segregation behavior of $La^{3+}$ and $Gd^{3+}$ impacts both sintering and grain growth.

During grain growth, the $La^{3+}$ segregation causes solute drag resulting in less grain growth then in undoped and $Gd^{3+}$-doped yttria.[57,58] This is very similar to zirconia: $Ce^{4+}$ (isovalent, low size mismatch) does not segregate and results in coarse microstructures, while $Y^{3+}$ (aliovalent, large size mismatch) results in solute drag and fine-grained microstructures.[10–12,59] Similar effects were observed for $Al_2O_3$,[15] $SrTiO_3$,[60] and $BaTiO_3$.[61] For the present experiments, additional retarding effects on grain boundary migration arise from pore drag as discussed later.
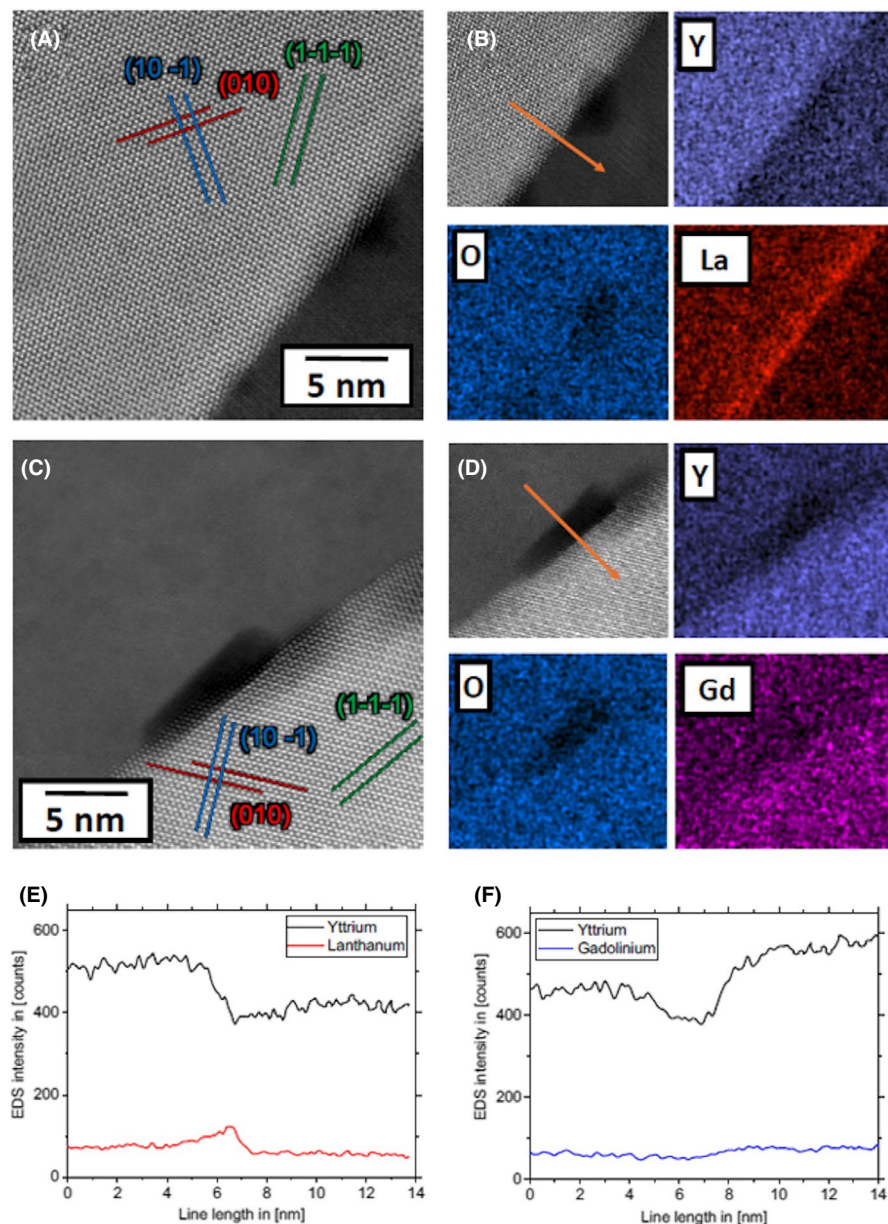
**FIGURE 9** Microstructure and chemical composition at the grain boundaries of 1 mol% $LaY_2O_3$ and 1 mol% $GdY_2O_3$ FAST/SPS-sintered at 1400°C, 120 min under 50 MPa. (A) HAADF image showing a grain boundary in $1LaY_2O_3$. (B) STEM-EDX mapping displaying the elemental distribution in $1LaY_2O_3$. (C) HAADF image showing a grain boundary in $1GdY_2O_3$. (D) STEM-EDX mapping displaying the elemental distribution in $1GdY_2O_3$. (E) EDS line scan taken from the HAADF image in (B) highlighting La segregation at the grain boundary. (F) EDS line scan taken from the HAADF image in (D) highlighting even Gd distribution across the grain boundary [Color figure can be viewed at wileyonlinelibrary.com]

For sintering, the impact of dopant segregation is more complex. The lower sintering activity of $La^{3+}$-doped yttria is likely caused by a decrease in grain boundary diffusion. In the metal community, it is well known that impurity segregation can decrease the grain boundary self-diffusion drastically.[39,62–65] The same effect was observed for alumina, where $Mg^{2+}$ segregation results in slower diffusion and higher creep resistance.[66,67] For $SrTiO_3$, Fe segregation was shown to decrease the sintering activity as well,[60] and the same was found for Y segregation in zirconia.[59] For yttria, Yoshida et al. documented a different impact of isovalent dopants on sintering: smaller dopants (compared to the host lattice site) increased the sintering rate, while larger dopants decreased it (Figure 2 in Ref. [36]). While not for all dopants, the segregation behavior was investigated, the findings agree well with the present dataset and the overall

picture of the literature. Overall, all these observations draw a consistent picture—a segregation of large isovalent dopants decreases the grain boundary diffusion and, hence, the sintering rates.

The reason for this relationship is not clear. Possibly, large, segregated ions at grain boundaries result in less open space available for diffusion. Another possibility is a change of the bonding structure at the grain boundary, where stronger bonds increase the thermal activation needed for diffusion.[36] Note that this is consistent with the higher activation energy for grain growth as evident in Figure 5. In any case, it can be concluded that grain boundary segregation of La has two consequences for microstructure evolution in yttria. First, the grain boundary migration is decreased by solute drag. Second, sintering rates are reduced by a decreased grain boundary diffusion.

In addition to solute drag, the presence of nano-sized pores seaming the grain boundaries might induce additional drag forces onto grain boundary motion which lead to the observed behavior in Section 3.2. Despite the high driving force for further shrinkage pores of this size exhibit, long dwell times at high temperatures seem not remove these features. Therefore, additional to HAADF imaging, EDS spectra of the nanoporosity and the adjacent host lattice were compared, and no impurity phases could be detected, and the interfacial porosity revealed the lowest EDS intensity (detailed analysis in Figure S3). The formation of nanopores is most likely caused by the specific processing conditions used in this study. Even if the exact origin of nanoporosity is difficult to determine, three possibilities exist to our understanding. Nanopores might be caused by entrapped carbon oxides formed from carbon depositions on the grain boundaries. Such residuals might be induced by carbon evaporation from graphite tools/graphite paper during the fast heating in the early stages of sintering. Also, residuals from the doping process, which are expected to be mainly located on grain boundaries, might act in a similar way. This assumption is supported by the lack of interfacial porosity in the case of pure $Y_2O_3$. Finally, gas entrapment from the chamber atmosphere might be another reason, but application of mild vacuum (<0.5 mbar) during FAST/SPS makes the effect the least likely. In all three cases, the low diffusion rate through the lattice prevents gas removal from the closed porosity and leads to a stabilization against further pore shrinkage. As sintering for the different compositions in this study is slightly different, the amount of carbon evaporating into the sample likely is different, yielding in a different number of nanopores documented in Figure 7. This phenomenon has been described for several ceramic material systems like $Al_2O_3$,[68,69] $ZrO_2$,[68] and $MgAl_2O_4$[70,71] during hot pressing and FAST/SPS densification. The hereby generated nanoporosity is under high internal pressures which can have a detrimental effect on the mechanical properties.

The grain boundary porosity generated during sintering of doped $Y_2O_3$ induces an additional drag force on the grain boundary mobility (pore drag[72–74]). This further reduces grain boundary kinetics which can be observed during grain growth in FAST/SPS (Figure 4) and mobility measurements in air (Figure 5). The presence of nanoporosity and the dopant-specific segregation behavior discovered by HR-STEM investigations may lead to the stepwise retardation of grain growth during densification (Figure 2) and isothermal grain growth (Figure 4) described in Section 3.1 with $La^{3+}$ doping showing the strongest drag effect due to a combined effect of pore and grain boundary segregation drag.

The grain boundary mobility of pure $Y_2O_3$ and $1LaY_2O_3$ determined in this study is summarized and compared to literature data in Figure 10 (adapted and edited from Ref. [43]). The measured kinetic data fit in the range of mobility data that have been found and discussed in various
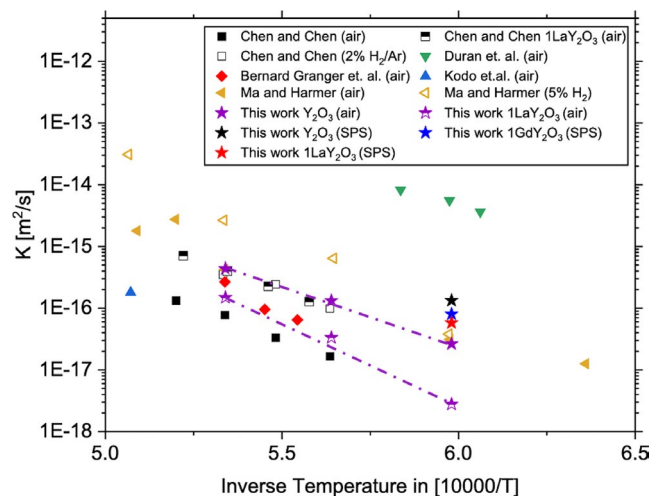


**FIGURE 10** Grain boundary mobility dependent on the inverse annealing temperature determined in this work in comparison to literature data.[29,31,35,43,75,76] All samples were fully densified by FAST/SPS before conducting the thermal treatment in air. The grain boundary mobility was calculated using Equation (2) [Color figure can be viewed at wileyonlinelibrary.com]

studies.[29,31,35,43,75,76] Several observations can be derived from the comparison to literature: The kinetic data reported by Duran et al. show a very high grain boundary mobility at low temperatures which could be connected to an undefined amount of impurities in the investigated powders.[75]

Nevertheless, the reported values for the grain boundary mobility of high-purity $Y_2O_3$ in air are the highest upon all other reported values. Furthermore, the grain boundary mobility of 1 mol% $La^{3+}$-doped $Y_2O_3$ shows an opposite behavior compared to the study of Chen and Chen.[29] They observed a positive influence of trivalent cation (especially $La^{3+}$) doping on the mobility of $Y_2O_3$ in air. Despite showing comparable values to Chen and Chen's work, the grain boundary mobility of 1 mol% $La^{3+}$ doped $Y_2O_3$ investigated in our study displays lower values compared to the corresponding pure $Y_2O_3$. This opposite behavior could be induced by the formation of nanoporosity at the grain boundaries due to the specific processing conditions used in our study. In contrast to the present work, Chen and Chen synthesized doped $Y_2O_3$ powders directly from nitrate precursors leading to a more homogenous dopant distribution which is not the case in nitrate precursor-coated powders. Overall, the high mobility values observed in the present study could be caused by the high relative density of investigated samples after FAST/SPS and the low amount of impurities in the starting powder (Table 1).

## 4 | SUMMARY AND CONCLUSIONS

The impact of segregation on sintering and grain growth was investigated in yttria. The focus was on segregation driven

by elastic effects, that is the size mismatch of dopants. In this light, sintering and grain growth kinetics of trivalent rare earth ($La^{3+}$, $Gd^{3+}$)-doped $Y_2O_3$ were investigated using sintering trajectories and grain growth experiments. Sintering was done by FAST/SPS.

During densification, two major effects were observed. First, doping with both cations lead to reduced grain coarsening during densification. Second, up to a temperature of 1300°C, doping with $La^{3+}$ strongly retarded the densification of $Y_2O_3$ requiring an approximately 100°C higher sintering temperature to achieve the same density compared to undoped $Y_2O_3$. This effect is connected to the different segregation behavior of $La^{3+}$ and $Gd^{3+}$ in the $Y_2O_3$ polycrystal. STEM-EDX investigations revealed a strong segregation of $La^{3+}$ to the grain boundary, which is caused by the size mismatch of $La^{3+}$ on the $Y^{3+}$ site. $Gd^{3+}$ does not segregate, as the size mismatch is only minor, and the grain boundary structures were not changed by doping of either $La^{3+}$ or $Gd^{3+}$. The low sintering rates of La-doped yttria are likely a consequence of segregation. The segregation seems to cause a decreasing grain boundary self-diffusion coefficient, possibly due to a change of the grain boundary structure or bonding state. This effect is known for other ceramics and metals.

Grain growth kinetics were studied for undoped and $La^{3+}$/$Gd^{3+}$-doped $Y_2O_3$ during FAST/SPS at constant temperature (1400°C) and varying dwell times (30–120 min) as well as in separate annealing experiments at varying temperatures (1400–1600°C) at constant dwell time (10 h) in air. Doping $Y_2O_3$ with 1 mol% $Gd^{3+}$ and $La^{3+}$ reduced the grain growth rates. This effect was much more pronounced for La doping. This can be explained by a solute drag effect induced by dopant segregation at the grain boundaries of $La^{3+}$-doped $Y_2O_3$ and the formation of nanoporosity located at the grain boundaries in both compounds.

The presence of nanoporosity at the grain boundaries was observed for both $Gd^{3+}$- and $La^{3+}$-doped yttria (not for undoped yttria). Three possible reasons of nanoporosity formation are discussed. There might be a carbon uptake during processing, which originates from the tool setup, for example through evaporation. If carbon residues inside the powder compact evaporate during later stage of the sintering, this might cause the formation of thermodynamically unfavorable grain boundary pores. Secondly, residuals from the doping process might act in a similar way. As third reason, due to relatively fast densification, gas species from the surrounding atmosphere might be entrapped in the sample. Due to conducting the FAST/SPS cycles in mild vacuum (<0.5 mbar), the last reason is quite unlikely. The nanoporosity results in an additional drag force on the grain boundary motion reducing the grain growth rates for both dopants. Accordingly, the grain growth rates in yttria decrease slightly for $Gd^{3+}$ doping and strongly for $La^{3+}$ doping, as in the latter case, solute drag

and pore drag are both active, while $Gd^{3+}$ doping only results in pore drag due to a lack of $Gd^{3+}$ segregation.

The superposition of several effects makes it challenging to draw final conclusions on the main mechanism of retarding grain growth especially during the early stages of sintering. Nevertheless, we believe that our results are of more general (and practical) interest for processing yttria ceramics fulfilling the challenging requirements of semiconductor industry. Therefore, our findings can be used to tailor microstructure evolution in yttria. While undoped $Y_2O_3$ showed preferentially intragranular pores, doping of $Y_2O_3$ with $La^{3+}$ reliably avoided the detachment of pores from the grain boundaries by the reduced grain boundary mobility, which enables to eliminate pores until the end of the final sintering stage reducing the porosity to a minimum. Such doped $Y_2O_3$-based ceramics have a high potential for application in the semiconductor industry due to the increased chemo-physical stability in contact with erosive plasma environments. In this context, $Gd^{3+}$ and $La^{3+}$ are attractive candidates for doping since they are classified as uncritical elements with respect to contamination during the plasma treatment.

## ORCID

_Moritz Kindelmann_ https://orcid.org/0000-0001-9676-2090
_Ke Ran_ https://orcid.org/0000-0002-9762-4586
_Wolfgang Rheinheimer_ https://orcid.org/0000-0002-2906-4265
_Koji Morita_ https://orcid.org/0000-0001-6040-7054
_Joachim Mayer_ https://orcid.org/0000-0003-3292-5342
_Martin Bram_ https://orcid.org/0000-0002-1203-2777
_Olivier Guillon_ https://orcid.org/0000-0003-4831-5725

## REFERENCES

1. Kirchheim R. Reducing grain boundary, dislocation line and vacancy formation energies by solute segregation. I. Theoretical background. Acta Mater. 2007;55(15):5129–38. https://doi.org/10.1016/j.actamat.2007.05.047

2. Amram D, Schuh CA. Interplay between thermodynamic and kinetic stabilization mechanisms in nanocrystalline Fe-Mg alloys. Acta Mater. 2018;144:447–58. https://doi.org/10.1016/j.actamat.2017.11.014

3. Raabe D, Herbig M, Sandlöbes S, Li Y, Tytko D, Kuzmina M, et al. Grain boundary segregation engineering in metallic alloys: a

pathway to the design of interfaces. Curr Opin Solid State Mater Sci. 2014;18(4):253–61. https://doi.org/10.1016/j.cossms.2014.06.002

4. Yan MF, Cannon RM, Bowen HK. Space-charge, elastic field, and dipole contributions to equilibrium solute segregation at interfaces. J Appl Phys. 1983;54(2):764–78. https://doi.org/10.1063/1.332035

5. Kim D, Bliem R, Hess F, Gallet J-J, Yildiz B. Electrochemical polarization dependence of the elastic and electrostatic driving forces to aliovalent dopant segregation on $LaMnO_3$. J Am Chem Soc. 2020;142(7):3548–63. https://doi.org/10.1021/jacs.9b13040

6. Kingery WD. Plausible concepts necessary and sufficient for interpretation of ceramic grain-boundary phenomena: I grain-boundary characteristics, structure and electrostatic potential. J Am Ceram Soc. 1974;57(1):1–8.

7. Kingery WD. Plausible concepts necessary and sufficient for interpretation of ceramic grain-boundary phenomena: II, solute segregation, grain-boundary diffusion and general discussion. J Am Ceram Soc. 1974;57(2):74–83.

8. Gregori G, Merkle R, Maier J. Ion conduction and redistribution at grain boundaries in oxide systems. Prog Mater Sci. 2017;89:252–305. https://doi.org/10.1016/j.pmatsci.2017.04.009

9. Matsui K, Yoshida H, Ikuhara Y. Review: microstructure-development mechanism during sintering in polycrystalline zirconia. Int Mater Rev. 2018;63(6):375–406. https://doi.org/10.1080/09506608.2017.1402424

10. Hwang S-L, Chen IW. Grain size control of tetragonal zirconia polycrystals using the space charge concept. J Am Ceram Soc. 1990;73(11):3269–77. https://doi.org/10.1111/j.1151-2916.1990.tb06449.x

11. Boulc'h F, Djurado E, Dessemond L. Dopant segregation and space charge effect in nanostructured tetragonal zirconia. J Electrochem Soc. 2004;151(8):A1210. https://doi.org/10.1149/1.1764711

12. Zhang F, Vanmeensel K, Batuk M, Hadermann J, Inokoshi M, Van Meerbeek B, et al. Highly-translucent, strong and aging-resistant 3Y-TZP ceramics for dental restoration by grain boundary segregation. Acta Biomater. 2015;16:215–22.

13. Subramaniam A, Koch CT, Cannon RM, Rühle M. Intergranular glassy films: an overview. Mater Sci Eng A. 2006;422(1–2):3–18.

14. Dillon SJ, Tang M, Carter WC, Harmer MP. Complexion: a new concept for kinetic engineering in materials science. Acta Mater. 2007;55(18):6208–18. https://doi.org/10.1016/j.actamat.2007.07.029

15. Fang J, Thompson AM, Harmer MP, Chan HM. Effect of yttrium and lanthanum on the final-stage sintering behavior of ultrahigh-purity alumina. J Am Ceram Soc. 1997;80(8):2005–12. https://doi.org/10.1111/j.1151-2916.1997.tb03084.x

16. Miwa K, Takada N, Sasaki K. Fluorination mechanisms of $Al_2O_3$ and $Y_2O_3$ surfaces irradiated by high-density $CF_4/O_2$ and $SF_6/O_2$ plasmas. J Vac Sci Technol A Vacuum, Surfaces, Film. 2009;27(4):831–5. https://doi.org/10.1116/1.3112624

17. Kim D-M, Lee S-H, Alexander WB, Kim K-B, Oh Y-S, Lee S-M. X-ray photoelectron spectroscopy study on the interaction of yttrium-aluminum oxide with fluorine-based plasma. J Am Ceram Soc. 2011;94(10):3455–9. https://doi.org/10.1111/j.1551-2916.2011.04589.x

18. Kindelmann M, Stamminger M, Schön N, et al. Erosion behavior of $Y_2O_3$ in fluorine-based etching plasmas: orientation dependency and reaction layer formation. J Am Ceram Soc. 2020. https://doi.org/10.1111/jace.17556

19. Jorgensen PJ, Anderson RC. Grain-boundary segregation and final-stage sintering of $Y_2O_3$. J Am Ceram Soc. 1967;50(11):553–8.

20. Rhodes WH. Controlled transient solid second-phase sintering of yttria. J Am Ceram Soc. 1981;64(1):13–9. https://doi.org/10.1111/j.1151-2916.1981.tb09551.x

21. Podowitz SR, Gaumé R, Feigelson RS. Effect of europium concentration on densification of transparent $Eu:Y_2O_3$ scintillator ceramics using hot pressing. J Am Ceram Soc. 2010;93(1):82–8. https://doi.org/10.1111/j.1551-2916.2009.03350.x

22. Yoshida H, Morita K, Kim B-N, Soga K, Yamamoto T. Production of transparent yttrium oxide ceramics by the combination of low temperature spark plasma sintering and zinc cation-doping. J Eur Ceram Soc. 2018;38(4):1972–80.

23. Furuse H, Nakasawa S, Yoshida H, et al. Transparent ultrafine $Yb^{3+}:Y_2O_3$ laser ceramics fabricated by spark plasma sintering. J Am Ceram Soc. 2018;101(2):694–702. https://doi.org/10.1111/jace.15232

24. Katayama K, Õsawa H, Akiba T, Urabe K, Yanagida H. Sintering of yttrias with addition of divalent metal oxide and water vapour pressure dependence of their electrical conductivity. J Mater Sci. 1990;25(2):1503–8. https://doi.org/10.1007/BF00585473

25. Katayama K, Osawa H, Akiba T, Yanagida H. Sintering and electrical properties of CaO-doped $Y_2O_3$. J Eur Ceram Soc. 1990;6(1):39–45. https://doi.org/10.1016/0955-2219(90)90033-C

26. Jorgensen PJ, Westbrook JH. Role of solute segregation at grain boundaries during final-stage sintering of alumina. J Am Ceram Soc. 1964;47(7):332–8. https://doi.org/10.1111/j.1151-2916.1964.tb12996.x

27. Baumard JF, Vesteghem H, Gasgnier G, Boncoeur M, Bougoin M. Densification of yttria ceramics. Adv Mater Res. 1994;1–2:47–54. https://doi.org/10.4028/www.scientific.net/AMR.1-2.47

28. Gasgnier G, Baumard JF, Boncoeur M, Bougoin M. Enhanced densification of yttria by addition of titanium oxide. J Eur Ceram Soc. 1994;13(1):67–72. https://doi.org/10.1016/0955-2219(94)90060-4

29. Chen P, Chen I. Grain boundary mobility in $Y_2O_3$: defect mechanism and dopant effects. J Am Ceram Soc. 1996;79(7):1801–9.

30. Busker G, Chroneos A, Grimes RW, Chen I. Solution mechanisms for dopant oxides in yttria. J Am Ceram Soc. 1999;82(6):1553–9.

31. Chen I-W. Grain boundary kinetics in oxide ceramics with the cubic fluorite crystal structure and its derivatives. Interface Sci. 2000;8(2):147–56. https://doi.org/10.1023/a:1008742404071.

32. Chen I-W, Wang X-H. Sintering dense nanocrystalline ceramics without final-stage grain growth. Nature. 2000;404(6774):168–71.

33. Wang X, Chen P, Chen I. Two-step sintering of ceramics with constant grain-size, I. $Y_2O_3$. J Am Ceram Soc. 2006;89(2):431–7.

34. Kodo M, Soga K, Yoshida H, Yamamoto T. Low temperature sintering of polycrystalline yttria by transition metal ion doping. J Ceram Soc Japan. 2009;117(1366):765–8.

35. Kodo M, Soga K, Yoshida H, Yamamoto T. Doping effect of divalent cations on sintering of polycrystalline yttria. J Eur Ceram Soc. 2010;30(13):2741–7. https://doi.org/10.1016/j.jeurceramsoc.2010.05.028

36. Yoshida H, Kodo M, Soga K, Yamamoto T. Doping effect on sinterability of polycrystalline yttria: from the viewpoint of cation diffusivity. J Eur Ceram Soc. 2012;32(12):3103–14. https://doi.org/10.1016/j.jeurceramsoc.2012.04.010

37. Kim D-M, Kim K-B, Yoon S-Y, Oh Y-S, Kim H-T, Lee S-M. Effects of artificial pores and purity on the erosion behaviors of polycrystalline $Al_2O_3$ ceramics under fluorine plasma. J Ceram Soc Japan. 2009;117(1368):863–7.

38. Ashizawa H, Yoshida K. Effect of the microstructures of yttria ceramics on their plasma corrosion behavior. Ceram Int.

2019;45(17):21162–7. https://doi.org/10.1016/j.ceramint.2019.07.093

39. Koju RK, Mishin Y. Atomistic study of grain-boundary segregation and grain-boundary diffusion in Al-Mg alloys. Acta Mater. 2020;201:596–603. https://doi.org/10.1016/j.actamat.2020.10.029

40. Foex M. Investigation on the melting point of yttrium oxide (possible secondary temperature standard). High Temp Press. 1977;9(3):269–82.

41. Gerlt ARC, Criner AK, Semiatin L, Payton EJ. On the grain size proportionality constants calculated in M.I. Mendelson's "Average Grain Size in Polycrystalline Ceramics". J Am Ceram Soc. 2019;102(1):37–41. https://doi.org/10.1111/jace.15950

42. Rahaman MN. Ceramic Processing and Sintering. Boca Raton, FL: CRC Press; 2003.

43. Ma S, Harmer MP. Near-intrinsic grain-boundary mobility in dense yttria. J Am Ceram Soc. 2011;94(3):651–5. https://doi.org/10.1111/j.1551-2916.2010.04351.x

44. Rheinheimer W, Bäurer M, Handwerker CA, Blendell JE, Hoffmann MJ. Growth of single crystalline seeds into polycrystalline strontium titanate: anisotropy of the mobility, intrinsic drag effects and kinetic shape of grain boundaries. Acta Mater. 2015;95:111–23. https://doi.org/10.1016/j.actamat.2015.05.019

45. Langer J, Hoffmann MJ, Guillon O. Direct comparison between hot pressing and electric field-assisted sintering of submicron alumina. Acta Mater. 2009;57(18):5454–65. https://doi.org/10.1016/j.actamat.2009.07.043

46. Langer J, Hoffmann MJ, Guillon O. Electric field-assisted sintering in comparison with the hot pressing of yttria-stabilized zirconia. J Am Ceram Soc. 2011;94(1):24–31. https://doi.org/10.1111/j.1551-2916.2010.04016.x

47. Chaim R, Shlayer A, Estournes C. Densification of nanocrystalline $Y_2O_3$ ceramic powder by spark plasma sintering. J Eur Ceram Soc. 2009;29(1):91–8. https://doi.org/10.1016/j.jeurceramsoc.2008.05.043

48. Yoshida H, Morita K, Kim B-N, Hiraga K, Yamanaka K, Soga K, et al. Low-temperature spark plasma sintering of yttria ceramics with ultrafine grain size. J Am Ceram Soc. 2011;94(10):3301–7. https://doi.org/10.1111/j.1551-2916.2011.04583.x

49. Sordelet DJ, Akinc M. Sintering of monosized, spherical yttria powders. J Am Ceram Soc. 1988;71(12):1148–53.

50. Wang SF, Zhang J, Luo DW, Gu F, Tang DY, Dong ZL, et al. Transparent ceramics: processing, materials and applications. Prog Solid State Chem. 2013;41(1):20–54. https://doi.org/10.1016/j.progsolidstchem.2012.12.002

51. Wynblatt P, Rohrer GS, Papillon F. Grain boundary segregation in oxide ceramics. J Eur Ceram Soc. 2003;23(15):2841–8. https://doi.org/10.1016/S0955-2219(03)00308-X

52. Lee W, Han JW, Chen Y, Cai Z, Yildiz B. Cation size mismatch and charge interactions drive dopant segregation at the surfaces of manganite perovskites. J Am Chem Soc. 2013;135(21):7909–25. https://doi.org/10.1021/ja3125349

53. Desu SB, Payne DA. Interfacial segregation in perovskites: I. Theory. J Am Ceram Soc. 1990;73(11):3391–7.

54. Tománek D, Aligia AA, Balseiro CA. Calculation of elastic strain and electronic effects on surface segregation. Phys Rev B. 1985;32(8):5051–6. https://doi.org/10.1103/PhysRevB.32.5051

55. Fabrichnaya O, Wang C, Zinkevich M, Aldinger F, Levi CG. Phase equilibria and thermodynamic properties of the $ZrO_2$-$GdO_{1.5}$-$YO_{1.5}$ system. J Phase Equilibria Diffus. 2005;26(6):591–604.

56. Fabrichnaya O, Zinkevich M, Aldinger F. Thermodynamic modelling in the $ZrO_2$–$La_2O_3$–$Y_2O_3$–$Al_2O_3$ system. Int J Mater Res. 2007;98(9):838–46. https://doi.org/10.3139/146.101539

57. Cahn JW. The impurity-drag effect in grain boundary motion. Acta Metall. 1962;10(9):789–98.

58. Vikrant KSN, Rheinheimer W, García RE. Electrochemical drag effect on grain boundary motion in ionic ceramics. npj Comput Mater. 2020;6(1):165.

59. Boutz MMR, Winnubst AJA, Burggraaf AJ. Yttria-ceria stabilized tetragonal zirconia polycrystals: Sintering, grain growth and grain boundary segregation. J Eur Ceram Soc. 1994;13(2):89–102. https://doi.org/10.1016/0955-2219(94)90106-6

60. Vikrant KSN, Rheinheimer W, Sternlicht H, Bäurer M, García RE. Electrochemically-driven abnormal grain growth in ionic ceramics. Acta Mater. 2020;200:727–34. https://doi.org/10.1016/j.actamat.2020.08.027

61. Rahaman MN, Manalert R. Grain boundary mobility of $BaTiO_3$ doped with aliovalent cations. J Eur Ceram Soc. 1998;18(8):1063–71. https://doi.org/10.1016/S0955-2219(97)00215-X

62. Esin VA, Souhar Y. Solvent grain boundary diffusion in binary solid solutions: a new approach to evaluate solute grain boundary segregation. Philos Mag. 2014;94(35):4066–79. https://doi.org/10.1080/14786435.2014.980043

63. Divinski SV, Reglitz G, Wilde G. Grain boundary self-diffusion in polycrystalline nickel of different purity levels. Acta Mater. 2010;58(2):386–95. https://doi.org/10.1016/j.actamat.2009.09.015

64. Herzig C, Divinski SV. Grain boundary diffusion in metals: recent developments. Mater Trans. 2003;44(1):14–27. https://doi.org/10.2320/matertrans.44.14

65. Bernardini J, Gas P, Hondros ED, Seah MP, Nicholson RB. The role of solute segregation in grain boundary diffusion. Proc R Soc London A Math Phys Sci. 1982;379(1776):159–78. https://doi.org/10.1098/rspa.1982.0011

66. Cho J, Rickman JM, Chan HM, Harmer MP. Modeling of grain-boundary segregation behavior in aluminum oxide. J Am Ceram Soc. 2000;83(2):344–52. https://doi.org/10.1111/j.1151-2916.2000.tb01196.x

67. Sakaguchi I, Srikanth V, Ikegami T, Haneda H. Grain boundary diffusion of oxygen in alumina ceramics. J Am Ceram Soc. 1995;78(9):2557–9. https://doi.org/10.1111/j.1151-2916.1995.tb08703.x

68. Morita K, Kim B-N, Yoshida H, Hiraga K, Sakka Y. Distribution of carbon contamination in oxide ceramics occurring during spark-plasma-sintering (SPS) processing: II-effect of SPS and loading temperatures. J Eur Ceram Soc. 2018;38(6):2596–604.

69. Bennison SJ, Harmer MP. Swelling of hot-pressed $Al_2O_3$. J Am Ceram Soc. 1985;68(11):591–7.

70. Morita K, Kim B-N, Yoshida H, Hiraga K, Sakka Y. Distribution of carbon contamination in $MgAl_2O_4$ spinel occurring during spark-plasma-sintering (SPS) processing: I–effect of heating rate and post-annealing. J Eur Ceram Soc. 2018;38(6):2588–95.

71. Morita K, Kim B-N, Hiraga K, Yoshida H. Fabrication of transparent $MgAl_2O_4$ spinel polycrystal by spark plasma sintering processing. Scr Mater. 2008;58(12):1114–7.

72. Hötzer J, Rehn V, Rheinheimer W, Hoffmann MJ, Nestler B. Phase-field study of pore-grain boundary interaction. J Ceram Soc Japan. 2016;124(4):329–39. https://doi.org/10.2109/jcersj2.15266

73. Rehn V, Hötzer J, Kellner M, et al. The impact of pores on microstructure evolution: a phase-field study of pore-grain boundary

interaction. In: Nagel WE, Kröner DH, Resch MM, editor. High Performance Computing in Science and Engineering '17. Cham: Springer International Publishing; 2018:485–502 pp. https://doi.org/10.1007/978-3-319-68394-2_29

74. Rehn V, Hötzer J, Rheinheimer W, Seiz M, Serr C, Nestler B. Phase-field study of grain growth in porous polycrystals. Acta Mater. 2019;174:439–49. https://doi.org/10.1016/j.actamat.2019.05.059

75. Duran P, Tartaj J, Moure C. Sintering behaviour of $Y_2O_3$ powders prepared by the polymer complex solution method. Ceram Int. 2002;28(7):791–803.

76. Bernard-Granger G, Guizard C, San-Miguel L. Sintering behavior and optical properties of yttria. J Am Ceram Soc. 2007;90(9):2698–702.

**SUPPORTING INFORMATION**
Additional supporting information may be found online in the Supporting Information section.